

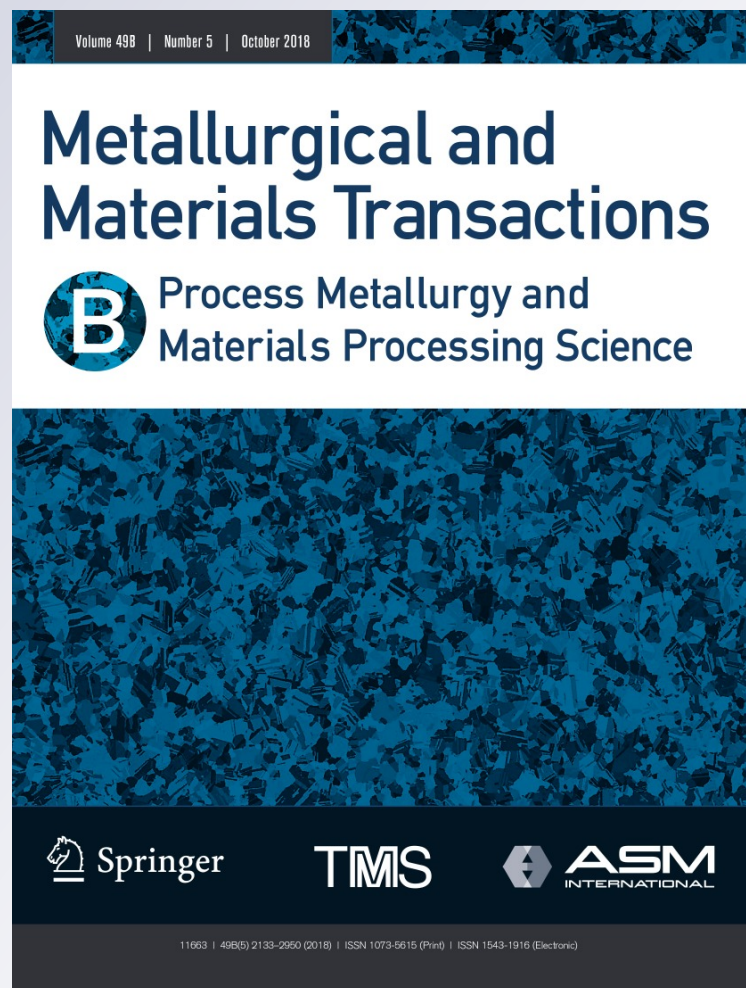
Simulation of Air Entrainment during Mold Filling: Comparison with Water Modeling Experiments

Seyyed Hojjat Majidi, John Griffin & Christoph Beckermann

**Metallurgical and Materials
Transactions B**

ISSN 1073-5615
Volume 49
Number 5

Metall and Materi Trans B (2018)
49:2599-2610
DOI 10.1007/s11663-018-1334-4



 Springer

Your article is protected by copyright and all rights are held exclusively by The Minerals, Metals & Materials Society and ASM International. This e-offprint is for personal use only and shall not be self-archived in electronic repositories. If you wish to self-archive your article, please use the accepted manuscript version for posting on your own website. You may further deposit the accepted manuscript version in any repository, provided it is only made publicly available 12 months after official publication or later and provided acknowledgement is given to the original source of publication and a link is inserted to the published article on Springer's website. The link must be accompanied by the following text: "The final publication is available at link.springer.com".

Simulation of Air Entrainment during Mold Filling: Comparison with Water Modeling Experiments



SEYYED HOJJAT MAJIDI, JOHN GRIFFIN, and CHRISTOPH BECKERMANN

Oxide inclusions form during pouring of metal castings as a result of air entrainment. Recently, a model was developed by the authors to predict the volumetric air entrainment during pouring. It was found that the velocity, diameter, and turbulence intensity of the liquid stream affect the air entrainment rate during pouring. In this study, the developed air entrainment model is validated with water modeling experiments. In the water modeling studies, water was poured using a bottom pour ladle. The effects of nozzle opening, head height, nozzle diameter, and nozzle extension are simulated. The predictions compare favorably with the experimental measurements. Results indicate that low head height and short pouring time have a beneficial effect on reducing the air entrainment during pouring. In addition, a fully open nozzle and the use of a nozzle extension further reduce the amount of entrained air.

<https://doi.org/10.1007/s11663-018-1334-4>

© The Minerals, Metals & Materials Society and ASM International 2018

I. INTRODUCTION

OXIDE inclusions are among the most commonly reported causes of repair in ferrous and non-ferrous castings.^[1,2] These inclusions affect the fatigue strength, fracture toughness, and machinability of a casting and may cause rejection of the cast part.^[1,3] Oxide inclusions form when the liquid metal comes into contact with oxygen during mold filling. In aluminum alloy castings, the exposure of liquid aluminum to the oxygen results in an extremely thin solid oxide film covering the liquid metal surface during mold filling. As the liquid metal experiences free surface turbulence, the dry side of an oxide covering the melt can come in contact with the dry side of another oxide, and form double oxide films or bifilms.^[1,4,5] In carbon and low alloy steel castings, steel reacts with oxygen to form oxide inclusions composed of the most reactive elements in the steel.^[2] These inclusions are typically called reoxidation inclusions. In ductile iron castings, magnesium oxide forms when the magnesium and oxygen react during magnesium treatment and filling. The subsequent reaction between the magnesium oxide and silicon oxide (silica) is responsible

for the formation of dross inclusions.^[3] Therefore, limiting the exposure of liquid metal to oxygen is necessary to minimize oxide inclusions.

Air entrainment is the major source of oxide inclusion formation during pouring of metal castings. In free surface flows, air is entrained once the liquid experiences surface turbulence. Such surface discontinuities are created, for example, by a liquid jet plunging into a pool, or a hydraulic jump where a fast moving liquid discharges into a low velocity atmosphere. For a plunging liquid jet (Figure 1), once the inertial force of the impinging liquid jet overcomes the restraining forces, including surface tension, air is entrained at the intersecting perimeter of the liquid jet and the pool. While several studies have proposed correlations for the entrainment onset based on the Reynolds and Weber numbers,^[6,7] Ervine *et al.*^[8] showed that the onset of the air entrainment depends on the turbulence level of the liquid jet. For turbulent water jets, air entrainment commences above approximately 1 m s^{-1} . Several experiments have been conducted to study the effect of different parameters on the air entrainment for a plunging liquid jet. Based on the results of the measurements, numerous correlations have been proposed for the relative air entrainment rate. Experimental studies have shown that increasing the liquid jet velocity significantly increases the air entrainment.^[9–11] Measurements have also demonstrated that the relative air entrainment increases with an increase in falling height, and decreases with an increase of the liquid jet diameter.^[8,10,11] In addition, the turbulence level of the liquid jet has been shown to have a significant effect on the air entrainment rate.^[8]

SEYYED HOJJAT MAJIDI and CHRISTOPH BECKERMANN are with the Department of Mechanical and Industrial Engineering, University of Iowa, Iowa City, IA 52242. Contact e-mail: becker@engineering.uiowa.edu JOHN GRIFFIN is with the Department of Material Science and Engineering, University of Alabama at Birmingham, Birmingham, AL 35294.

Manuscript submitted March 2, 2018.

Article published online July 10, 2018.

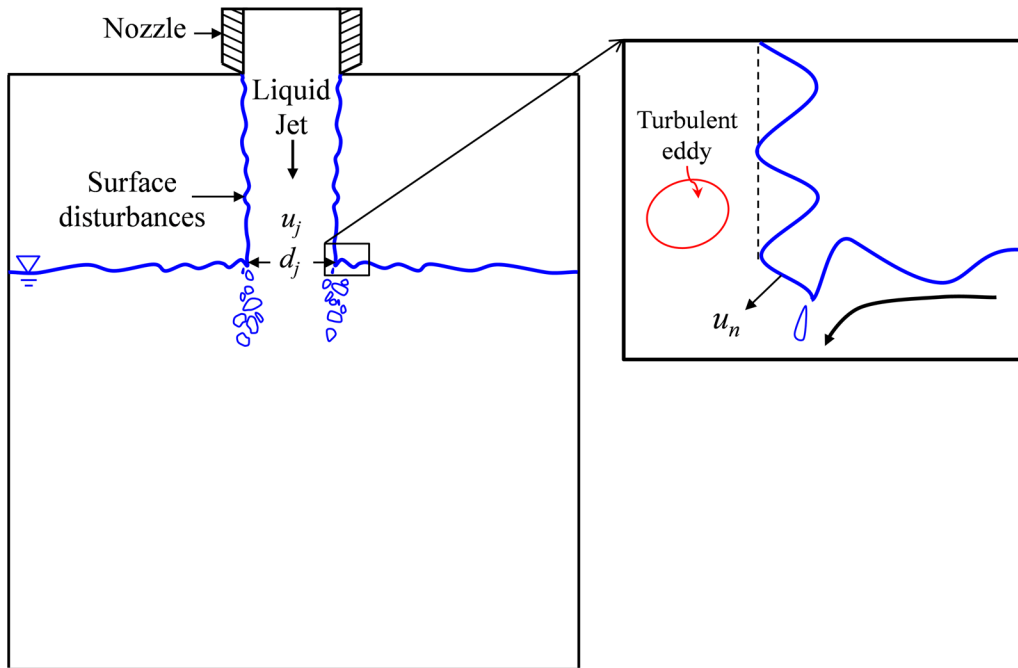


Fig. 1—Air bubbles near the impact location of a plunging liquid water jet. Free surface disturbances shown along the periphery of the liquid jet.

In metal castings, the pouring and gating system design affects the air entrainment during mold filling. Liquid metal plunging into the pouring cup or basin or flowing down the sprue are examples of air entrainment in the gating system. The oxygen inside the entrained air reacts immediately with the liquid metal to form oxide inclusions. These inclusions are then transported with the liquid metal and ultimately end up as non-metallic inclusions in the solidified casting. Large inclusions may accumulate on the cope surface if air entrainment is substantial.

Water modeling experiments are useful in understanding the effect of various gating designs and pouring conditions on the characteristics of the liquid metal flow and, consequently, air entrainment. Comparison between the results of water modeling experiments to those in liquid metal requires dynamic similarity. In steel, the kinematic viscosities of liquid steel and water are very similar.^[12,13] However, a full-scale water model is necessary to accurately simulate molten steel flow behavior. A full-scale water model will produce similar Reynolds and Froude numbers compared to molten steel.

Water is commonly used to model steel flow by the wrought steel industry.^[12] However, few water modeling experiments have been conducted to correlate the pouring parameters and conditions to air entrainment during the pouring of metal castings. The results of the water modeling studies conducted by Wanstall *et al.*^[12] and Bates and Griffin^[13] showed that a throttled bottom pour ladle entrains significantly more air compared to an open nozzle (unthrottled) configuration. In addition, results from this study indicate that shorter falling heights and filling times reduce the amount of entrained

air. Through a series of experiments, Kuyucak^[14] showed that using an offset pouring basin with a step before the sprue entrance allows the entrained air to escape to the atmosphere before entering the sprue. Additionally, the use of a nozzle extension submerged into the pouring basin significantly reduces the amount of entrained air during pouring. The benefit of using a submerged gate was also shown in the experiments conducted by Wang *et al.*^[15] Afsharpour *et al.*^[16] suggested that a conical pouring cup entrains large amount of bubbles, and using an offset step pouring basin and a small sprue reduces the air entrainment to a great extent.

The prediction of oxide inclusion formation requires a model to estimate the air entrainment during mold filling. Based on the work by Ma *et al.*,^[17] the authors have recently developed a model for predicting the local air entrainment rate.^[18] The model accounts for the free surface turbulence at the liquid–air interface. The sub-grid air entrainment model was implemented into a casting filling simulation code to calculate local air entrainment rates during filling. The ultimate goal is to apply the developed model to liquid metals, and predict the air entrainment during mold filling. However, before proceeding to liquid metals the air entrainment model must be validated with water modeling measurements. In the present study, the developed air entrainment model is validated by comparing the predicted relative air entrainment volumes with measured data from water modeling experiments.^[12,13] It is shown how different pouring conditions, such as throttling the nozzle, nozzle diameter, head height, and use of a nozzle extension for a bottom pour ladle, affect air entrainment.

II. AIR ENTRAINMENT MODEL

This section describes the model for predicting the local air entrainment rate at free surfaces. The air entrainment calculations described here are performed as part of a standard casting filling simulation.^[19] The filling simulation calculates the melt velocity by solving the Navier–Stokes equations at each time step, and the geometry of the free surface at each time step is determined using a volume tracking method.

Eddies in the turbulent flow raise disturbances on the periphery of the liquid jet, making the liquid–air interface rough (Figure 1). Air pockets are trapped inside these disturbances. Once air is entrained at the impact location, these air pockets are drawn into the bulk liquid where they are broken into smaller air bubbles and carried away with the liquid flow. In the developed model, the local air entrainment rate is a function of the turbulent kinetic energy, k , and the normal derivative of the normal component of the liquid velocity at the interface, $\partial u_n/\partial n$ ^[17]:

$$q = C_{\text{ent}} \frac{k \partial u_n}{g \partial n}, \quad [1]$$

where q is the volumetric air entrainment rate per unit interfacial area, C_{ent} is the entrainment coefficient, and g (m s^{-2}) is the gravitational acceleration. The gradient term determines the possibility of air entrainment. A positive gradient term, $\partial u_n/\partial n > 0$, implies that the liquid velocity is increasing away from the interface, drawing the air pockets into the bulk liquid. On the other hand, for a negative gradient term, $\partial u_n/\partial n < 0$, the air pockets will be detrained rather than entrained. Therefore, the only scenario where air can be entrained is for positive values of $\partial u_n/\partial n$. In the developed model, the turbulent kinetic energy is estimated from the sum of the squares of the fluctuating velocity components relative to a spatially averaged mean velocity.

For calculating the volumetric air entrainment rate, Q_a ($\text{m}^3 \text{s}^{-1}$), the air entrainment rate per unit interfacial area is integrated over the interfacial area, A_s

$$Q_a = \iint_{A_s} q dA. \quad [2]$$

The entrainment coefficient, $C_{\text{ent}} = 0.039$, was estimated by calibrating the predicted relative air entrainment rates with the experimental measurements reported in Reference 9 for plunging water jets with different liquid jet velocities and diameters at low turbulence intensities. Calculation of the turbulent kinetic energy, the normal derivative of the normal component of the liquid velocity at the interface, and the calibration of the entrainment coefficient are explained in detail in a previously published paper by Majidi and Beckermann.^[18] Using a single value of the air entrainment coefficient, a good agreement between measurements and predictions is achieved for plunging water jets with different liquid jet velocities, diameters, and turbulence intensities (Figure 2). In the plots, the

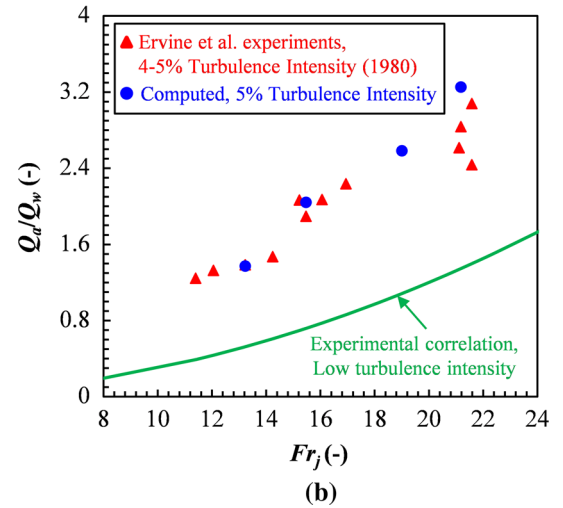
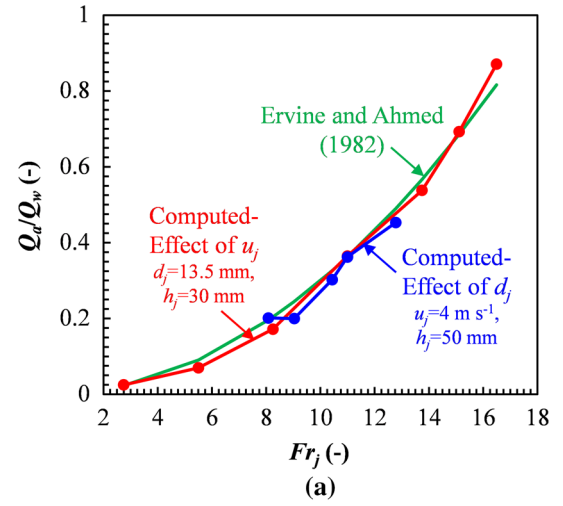


Fig. 2—Relative air entrainment rate as a function of Froude number for (a) low turbulence and (b) high turbulence plunging liquid jet.

Froude number at the impact location, Fr_j , is defined as follows:

$$Fr_j = \frac{u_j^2}{gd_j}, \quad [3]$$

where u_j (m s^{-1}) and d_j (m) are the velocity and diameter of liquid jet at impact, respectively. In the simulations, the turbulence intensity was induced by applying a time-dependent sinusoidal velocity profile at the nozzle exit. Results in Figure 2(b) show that the turbulence level of the plunging liquid jet significantly affects the air entrainment rate.

III. WATER MODELING EXPERIMENTS

In the water modeling experiments,^[12,13] water was poured using a bottom pour ladle to study the effects of different variables on air entrainment. References 12 and 13 are internal reports and have not been published in the open literature.

A. Experimental Apparatus

For the trials, a 508 mm (20") square by 660 mm (26") deep acrylic ladle with an effective volume of approximately 0.113 m^3 (4 ft^3) was used (Figure 3(a)). The ladle had a hole at the bottom where nozzles of different diameters were inserted.

The tank into which water was poured consisted of an acrylic box with a height and width of 457 mm and a length of 914 mm. Water was directly poured into the tank through the sprue. Water exiting the submerged sprue impinged on the quiescent water pool's surface. The water tank had a removable cover plate where sprues with different lengths and diameters could be inserted. The cover plate was sealed to the tank to prevent air leakage during pouring.

B. Measurements

The ladle weight was measured for each pour using a 454 kg (1000 pound) load cell attached to the ladle sling. Signals from the load cell, after amplification with a precision amplifier, were sent to a data acquisition board in a desktop computer. The difference between the static weight of the ladle at the beginning and at the end of the pour provided the total water volume poured.

The pouring time was measured using an electronic switch, which was installed on the lever of the stopper rod. The signals from the switch were sent to the data acquisition unit at the beginning and end of the pour, and the time difference between the start and end of each pour determined the pouring time.

Air is entrained when the water jet impinges on the quiescent pool surface (Figure 3(b)). In addition to the entrained air, the impinging water caused some air displacement. The displaced and entrained air was vented into a sealed bag at the top of the tank. Before each experiment, the bag was isolated from the water tank and a vacuum pump was used to remove air from the bag. The vacuum pressure was monitored with a water manometer. At the end of the pouring, the bag was again isolated from the fill box and the vacuum pump was used to pull air from the bag through a wet test meter to measure total volume of air. The pump was stopped once a low vacuum was detected. The wet gas meter was calibrated using air displaced by a known volume of water. The volume of entrained air was estimated as the difference between the total volume of collected air and the displaced air volume (determined from the volume of water poured).

The initial water level in the tank was 25.4 mm above the bottom of the sprue (h_{sub}) to seal the entrained air in the tank.

All the experimental results were expressed as the relative entrained air volume, *i.e.*, the ratio of the entrained air volume to the volume of water poured. Based on the precision of measurement devices, the relative air entrainment precision was between 2 pct (at the higher air entrainment rates) and 12 pct (at the

lowest observed rates). The experiments were repeated three times for each configuration to measure data variability under similar pouring conditions.

C. Experimental Variables

A variety of pouring parameters were studied. These parameters affect the velocity, diameter, falling height, and the turbulence intensity of the liquid jet. For each parameter, a high and a low value was considered. The effects of nozzle opening (open nozzle *vs* throttled nozzle), ladle depth, h_l , nozzle diameter, d_N , nozzle extension, h_{NE} , and sprue length, h_{sprue} , were studied (Figure 3(a)). Table I lists all of the cases studied for the bottom pour ladle. In all of the bottom pour ladle configurations, the distance between the ladle and the pouring cup was 76.2 mm. The nozzle opening was controlled by changing the stopper opening distance, h_{SO} , in Figure 3(a). For the open nozzle configurations, $h_{SO} = 63.5 \text{ mm}$, and $h_{SO} = 6.35 \text{ mm}$ for the throttled configurations. To study the effect of total head height on the air entrainment, two different ladle depths and two sprue lengths were studied. For the full ladle and half-full ladle, the liquid height inside the ladle was 660 and 279 mm, respectively. For the small nozzle diameter configurations ($d_N = 47.6 \text{ mm}$), a sprue diameter of $d_{sprue} = 50.8 \text{ mm}$ was used, while the sprue diameter was $d_{sprue} = 76.2 \text{ mm}$ for large nozzle diameter configurations ($d_N = 65.1 \text{ mm}$). For all configurations with the nozzle extension, a $h_{NE} = 127 \text{ mm}$ extension with the same diameter as the nozzle was added to the nozzle exit. For this purpose, the ladle was raised to maintain the height between the ladle and the pouring cup. The pouring times in Table I are calculated based on the three measured pouring time for pouring 0.029 m^3 (1 ft^3) of water. The standard deviations in Table I are calculated based on the three measured pouring times for each configuration. According to Table I, the standard deviations of the measured pouring times for the throttled nozzle configurations are significantly larger than the open nozzle cases. More details of the experiments can be found in References 12 and 13.

IV. SIMULATION OF WATER MODELING EXPERIMENTS

The developed air entrainment model was applied to the water modeling studies explained in Section III. For reducing the simulation time, a smaller water tank was utilized; the height and width (457 mm) were the same as the height and width of the water tank used in the above experiments, while the length of the tank was reduced from 914 to 660 mm (Figure 3(b)) for the simulations. However, the tank size was sufficiently large that the boundaries had no influence on the impact location at the water pool surface, where air entrainment occurs. Although the simulated water tank fills

Table I. Overview of the Measured and Simulated Configurations for Bottom Pour Ladle Water Modeling Experiments

Trial	Ladle Depth	Nozzle Diameter (mm)	Nozzle Extension	Sprue Length (m)	Pouring Time, t_{pour} (s)	Standard Deviation of Pouring Times, (-)	Friction Coefficient, C_f (-)	Measured Relative Air Entrainment, V_a/V_w (-)
<i>Open nozzle</i>								
1	full	47.6	no	0.13	5.12	0.003	0.93	0.171
2	full	47.6	no	0.26	5.12	1.2×10^{-5}	0.93	0.212
3	full	47.6	yes	0.13	5.68	0.002	0.85	0.147
4	full	47.6	yes	0.26	5.67	0.005	0.85	0.152
5	full	65.1	no	0.13	3.91	0.007	0.68	0.123
6	full	65.1	no	0.26	3.91	1.8×10^{-6}	0.68	0.147
7	half-full	47.6	no	0.13	8.37	0.014	0.99	0.107
8	half-full	47.6	no	0.26	8.36	0.021	0.99	0.18
9	half-full	47.6	yes	0.13	9.17	0.007	0.93	0.148
10	half-full	47.6	yes	0.26	9.17	0.011	0.93	0.206
11	half-full	65.1	no	0.13	6.22	0.013	0.78	0.11
12	half-full	65.1	no	0.26	6.25	0.017	0.78	0.148
<i>Throttled nozzle</i>								
13	full	47.6	no	0.13	12.2	0.106	0.48	0.655
14	full	47.6	no	0.26	12.2	0.013	0.48	0.97
15	full	47.6	yes	0.13	10.0	0.021	0.52	0.47
16	full	47.6	yes	0.26	9.95	0.007	0.52	0.718
17	full	65.1	no	0.13	7.9	0.003	0.42	0.583
18	full	65.1	no	0.26	7.85	0.055	0.42	0.519
19	half-full	47.6	no	0.13	21.2	0.141	0.59	0.47
20	half-full	47.6	no	0.26	20.6	0.019	0.60	0.392
20	half-full	47.6	yes	0.13	16.4	0.051	0.64	0.386
22	half-full	47.6	yes	0.26	18.5	0.033	0.61	0.575
23	half-full	65.1	no	0.13	13.8	0.053	0.60	0.467
24	half-full	65.1	no	0.26	13.9	0.265	0.60	0.507

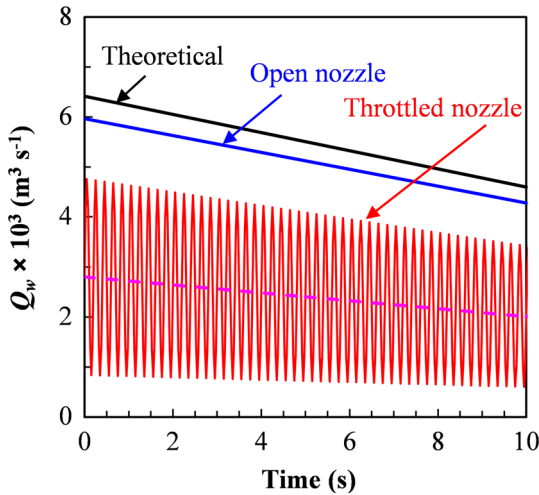


Fig. 4—Volumetric water flow rate as a function of time for the theoretical (no friction applied), open nozzle and throttled nozzle for the full ladle, small nozzle diameter, long sprue, and no nozzle extension configuration.

faster than the water tank used in the experiments, the water-level difference at the end of pouring is small (approximately 25.4 mm), and does not affect the simulation results. Similar to the experiments, in all configurations the sprue was submerged approximately 25.4 mm into the water. For all the cases, instead of modeling the ladle, the volumetric flow rate of water was

calculated and used as the input for the simulations. The thermo-physical properties of water at 298 K (25 °C) were used in the simulations.

Using the simplified energy conservation equation (Eq. [4]), *i.e.*, Bernoulli equation,^[20] and the continuity equation (Eq. [5]), an equation was derived for the liquid velocity at the nozzle exit, $u_{N,th}$:

$$u_{N,th} = \sqrt{2gh_l(t)} \quad [4]$$

$$-\frac{dh_l}{dt} \times A_{ladle} = A_N \times u_{N,th} \quad [5]$$

$$u_{N,th}(t) = \sqrt{2gh_{l,i}^{\frac{1}{2}} - g \frac{A_N}{A_{ladle}} t}, \quad [6]$$

where h_l (m) and $h_{l,i}$ (m) are the instantaneous and initial water height inside the bottom pour ladle, respectively, and A_N (m²) is the nozzle cross-sectional area

$$A_N = \frac{\pi}{4} d_N^2. \quad [7]$$

Based on the effective volume, $V_{ladle} = 0.113 \text{ m}^3$, and height of the bottom pour ladle, $h_{ladle} = 0.66 \text{ m}$, an equivalent ladle cross-sectional area was calculated as $A_{ladle} = V_{ladle}/h_{ladle} = 0.171 \text{ m}^2$.

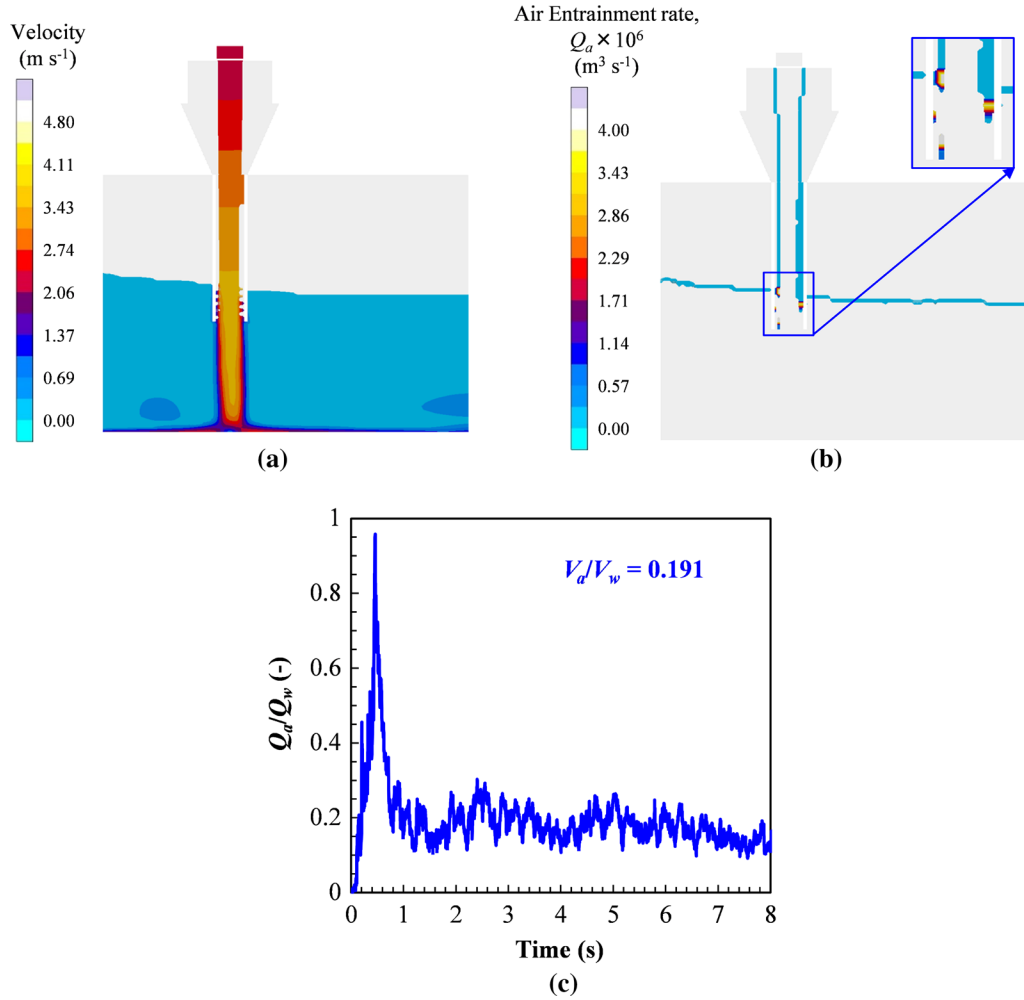


Fig. 5—Contours of (a) velocity and (b) local volumetric air entrainment rate, Q_a , at $t = 2$ s, and (c) total relative air entrainment rate as a function of time for the bottom pour ladle, open nozzle, half-full ladle, small nozzle diameter ($d_N = 47.6$ mm), long sprue ($h_{sprue} = 0.26$ m), and no nozzle extension configuration.

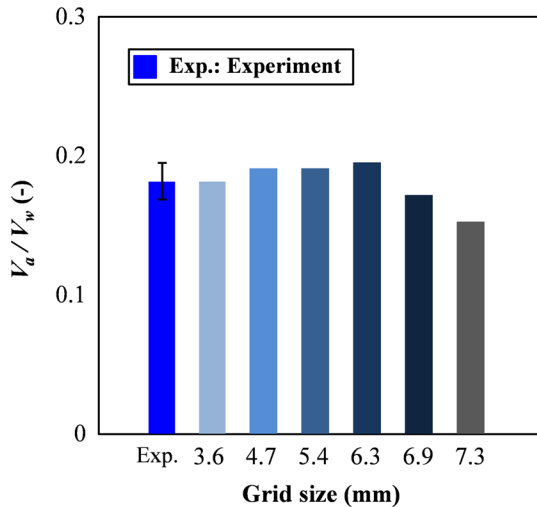


Fig. 6—Predicted relative air entrainment rate volume as a function of grid spacing for the bottom pour ladle, open nozzle, half-full ladle, small nozzle diameter ($d_N = 47.6$ mm), long sprue ($h_{sprue} = 0.26$ m), and no nozzle extension configuration.

In the simulations, a friction coefficient, C_f , was applied to the liquid velocity at the nozzle exit to account for the nozzle friction. The effective liquid velocity, $u_{N,eff}$, and volumetric flow rate are given as follows:

$$u_{N,eff}(t) = C_f \times u_{N,th}(t) \quad [8]$$

$$Q_w(t) = \frac{\pi}{4} d_N^2 u_{N,eff}(t). \quad [9]$$

To estimate the friction coefficient, first, the total volume of water poured was calculated by integrating the volumetric flow rate, Q_w , over the pouring time, t_{pour} :

$$V_w = \int_0^{t_{pour}} Q_w(t) dt = \frac{\pi}{4} d_N^2 \times C_f \int_0^{t_{pour}} u_{N,th}(t) dt. \quad [10]$$

Then, based on the reported pouring time for 0.029 m^3 of water, the friction coefficient, C_f , was calculated for each configuration. The calculated friction coefficients

are shown in Table I. The further a friction coefficient is below unity, the more friction is present in a nozzle.

According to the experimental observations of the throttled nozzle, the liquid at the nozzle exit had a large turbulence level. To model the throttled nozzle configurations, turbulence intensity was applied at the nozzle exit in the simulations. The turbulence intensity indicates the level of fluctuations in a turbulent flow and is defined as

$$I = \frac{\sqrt{u_{N,eff}^2}}{u_{N,eff}}, \quad [11]$$

where the prime and the overbar indicate the fluctuating and mean components of the liquid velocity at the nozzle exit, respectively. By applying turbulence intensity, the volumetric flow rate of water at the nozzle exit is calculated as

$$Q_w(t) = \frac{\pi}{4} d_N^2 u_{N,eff} [1 + I \times \sin(\pi \times f \times t)], \quad [12]$$

where f and t are the frequency of the fluctuations and time, respectively. Figure 4 compares the volumetric flow rate of water for the theoretical (friction coefficient not applied), open and throttled nozzle for the full ladle, small nozzle diameter, long sprue, and no nozzle extension configuration. Determination of the turbulence intensity and frequency for the throttled configurations is explained in Section V-B.

The large turbulence intensity at the nozzle exit generated large disturbances at the periphery of the liquid jet. The disturbances hitting the bottom of the pouring cup blocked the flow from entering to the sprue. This caused the water to overflow from the cup before the sprue was filled during the simulations for the small nozzle diameter configurations. Therefore, for the throttled small nozzle configurations, a sprue with slightly larger diameter, $d_{sprue} = 63.5$ mm, and a pouring cup with larger diameter were used in the simulations. Water did not overflow the cup in the simulations of the throttled large nozzle diameter cases; therefore, the diameter of the sprue and pouring cup was not changed for these configurations. Similar to the experiments, for all the bottom pour ladle trials the stream was centered above the sprue. For each of the open and throttled nozzles, the effects of ladle depth, nozzle diameter, sprue length, and nozzle extension were studied (Figure 3(b) and Table I).

V. RESULTS AND DISCUSSION

The velocity and local air entrainment contours of a base case (bottom pour ladle, open nozzle, half-full ladle, small nozzle diameter, long sprue, and no nozzle extension) are shown in Figure 5. As expected, the predicted local volumetric air entrainment rate contour shows that the air entrainment takes place at the periphery of the liquid jet where it plunges into the quiescent pool (Figure 5(b)). The total relative air entrainment rate plotted in Figure 5(c) indicates that

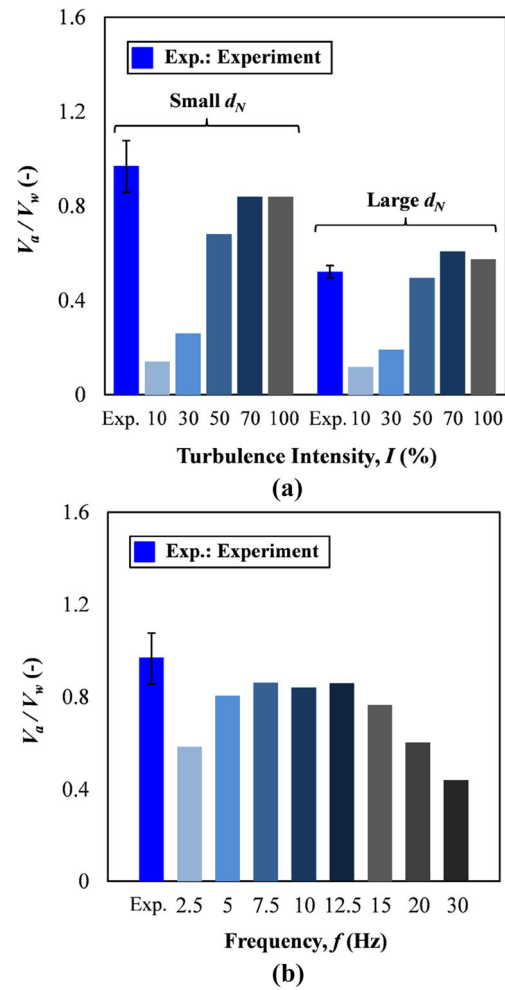


Fig. 7—Predicted relative air entrainment rate volume as a function of (a) turbulence intensity for the full ladle, long sprue ($h_{sprue} = 0.26$ m), and no nozzle extension configuration at a frequency of $f = 10$ Hz for small and large nozzle diameters, and (b) frequency for the full ladle, small nozzle diameter ($d_N = 47.6$ mm), long sprue ($h_{sprue} = 0.26$ m), and no nozzle extension configuration at turbulence intensity of $I = 70$ pct.

except for the first initial impact, where significant air is entrained, for the majority of pouring the relative air entrainment rate is approximately constant. Integrating the total volumetric air entrainment rate, Q_a , over time and dividing by the total volume of water poured, provides the relative air entrainment volume.

A. Mesh Independency

Before comparing the predicted results to the measurements for different configurations, a computational mesh dependency study was performed for the base case. In all cases, a uniform mesh was utilized that consists of cubes of a certain side length. Figure 6 shows that as the grid spacing is refined from a 7.3 to a 3.6 mm, the predicted relative air entrainment volume, V_a/V_w , experiences a slight change, though the total metal cells increase from 400,000 to 3,200,000. This

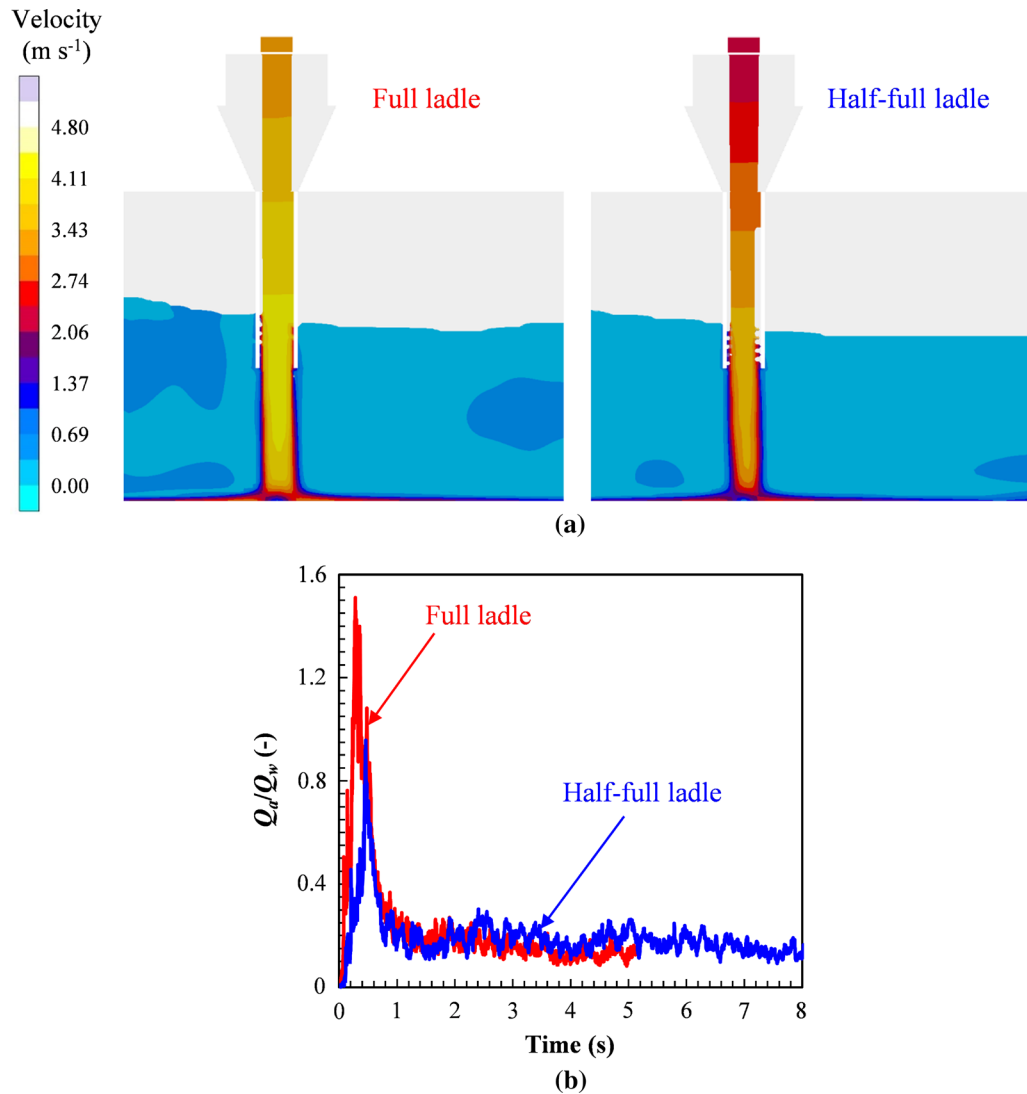


Fig. 8—Effect of the ladle depth on the variation of the relative air entrainment rate for open stopper, small nozzle diameter ($d_N = 47.6$ mm), long sprue ($h_{sprue} = 0.26$ m), and no nozzle extension configuration: (a) The velocity contours at time of $t = 2$ s for full ladle (left) and half-full ladle (right), and (b) relative air entrainment rate.

relatively minor mesh dependency is acceptable. For all of the following configurations, a uniform grid spacing of 6.3 mm is used.

B. Determination of the Turbulence Intensity and Frequency for Throttled Nozzle Configurations

As mentioned earlier, while zero turbulence intensity is applied for the open nozzle configurations in the simulations, throttled nozzle cases are modeled by applying turbulence intensity at the nozzle exit (Eq. [12]). To determine the turbulence intensity for the throttled nozzle configurations, two configurations—full ladle, long sprue, no nozzle extension, with small and large nozzle diameters—were simulated with different turbulence levels and compared with the experimental measurements. Figure 7(a) compares the measured and predicted relative air entrainment for five different turbulence intensities at a frequency of $f =$

10 Hz. Results show that increasing the turbulence intensity above 50 pct does not significantly affect the relative entrained air volume.

In addition, a frequency dependency was studied for the full ladle, small nozzle diameter, long sprue, and no nozzle extension configuration at a turbulence intensity of $I = 70$ pct (Figure 7(b)). Results indicate that the relative air entrainment volumes are independent of the frequency in the range of $5 \leq f(\text{Hz}) \leq 15$. Finally, a turbulence intensity of $I = 70$ pct and frequency of $f = 10$ Hz were selected for all of the throttled cases.

C. Comparison of Measurements and Predictions

Figure 8 shows the predicted relative air entrainment rate for two ladle depths. The comparison is made for the open nozzle, small nozzle diameter, long sprue, and no nozzle extension case. Once the liquid jet impinges into the water pool, air is entrained at

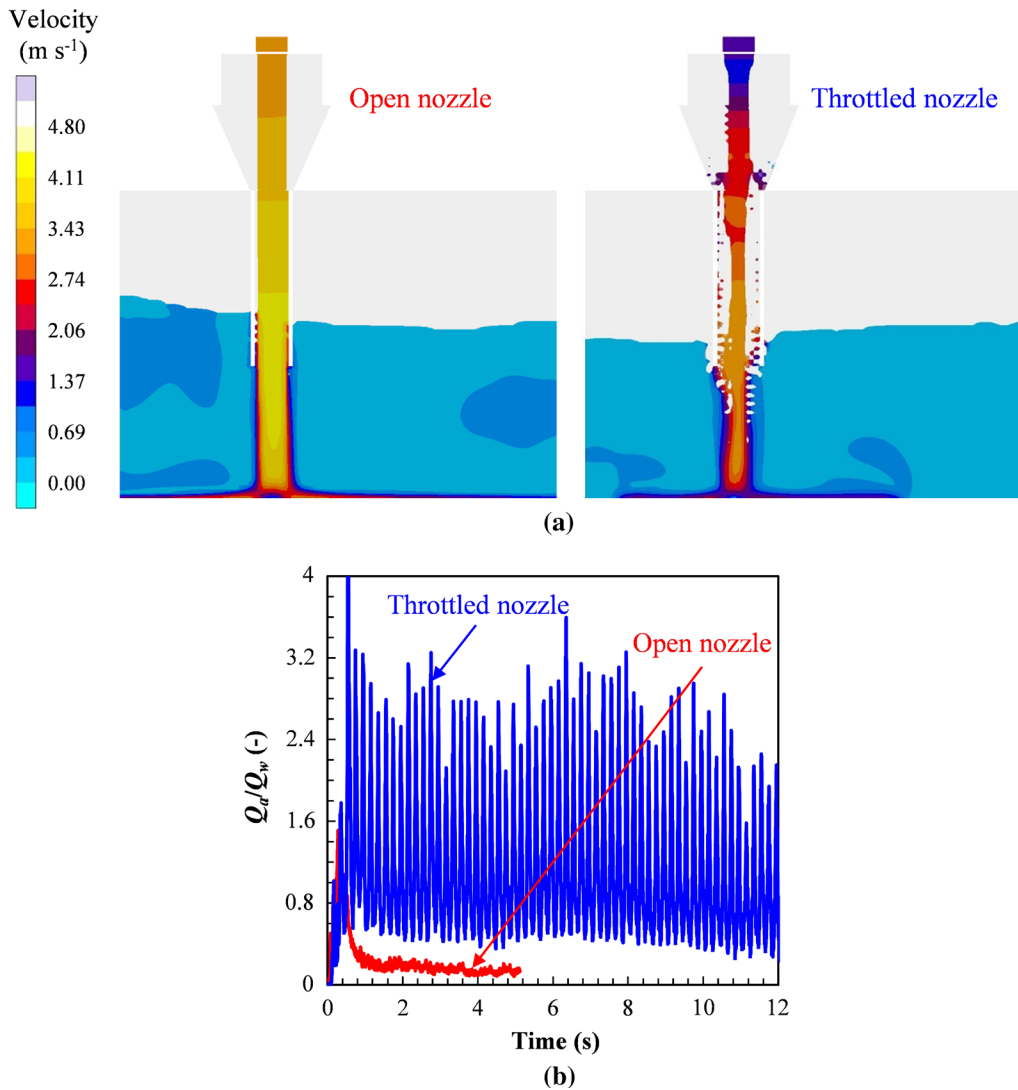


Fig. 9—Effect of the nozzle opening on the variation of the relative air entrainment rate for full ladle, small nozzle diameter ($d_N = 47.6$ mm), long sprue ($h_{sprue} = 0.26$ m), and no nozzle extension configuration: (a) The velocity contours at time of $t = 2$ s for open nozzle (left) and throttled nozzle (right), and (b) relative air entrainment rate.

the impact location. The large initial spike is due to the initial impact of the liquid jet on the water pool; this spike is larger for the full ladle configuration. A higher head height of liquid inside the ladle produces more hydrostatic pressure above the nozzle and, consequently, a higher liquid velocity at the nozzle exit. A higher exit velocity results in a higher liquid jet impact velocity, which leads to a higher air entrainment rate. After the initial spike, the relative air entrainment rate decreases as the water tank is filled. The decrease is more pronounced for the full ladle since the water tank is filled faster than the half-full ladle case. As mentioned earlier, zero turbulence intensity is applied at the nozzle exit for the open nozzle configurations. Therefore, the fluctuations during this period are generated due to unsteadiness of the flow.

Figure 9 compares the velocity contours and air entrainment predictions for the open nozzle and throttled nozzle. The comparison is made for the full ladle, small nozzle diameter, long sprue, and no nozzle extension configurations. Throttling the nozzle reduces the liquid velocity at the nozzle exit (Figure 9(a)); this is shown through the decrease in the friction coefficient in Table I. On the other hand, throttling the nozzle increases the turbulence intensity of the liquid jet at the nozzle exit, which increases the size of the disturbances on the liquid jet periphery, thereby increasing the air entrainment rate at the impingement point. Figure 9(b) indicates the effect of increased turbulence intensity outweighs the effect of reduced liquid jet velocity. Throughout the pouring, the air entrainment rate is significantly larger for the throttled nozzle than for the open nozzle configuration.

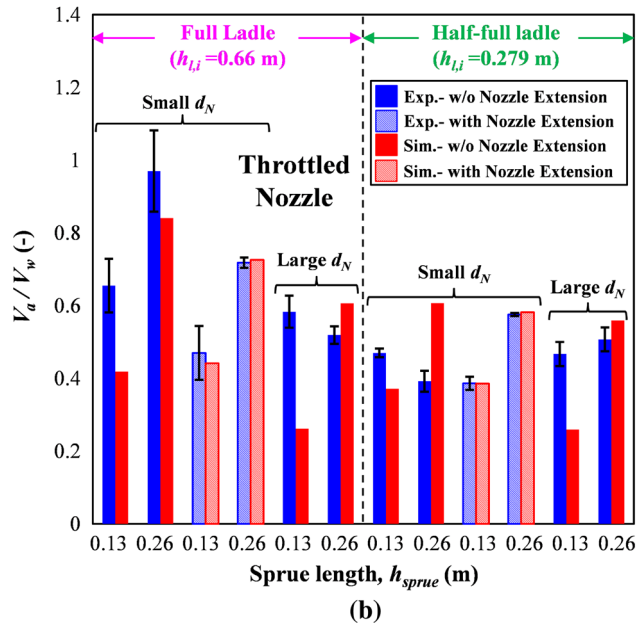
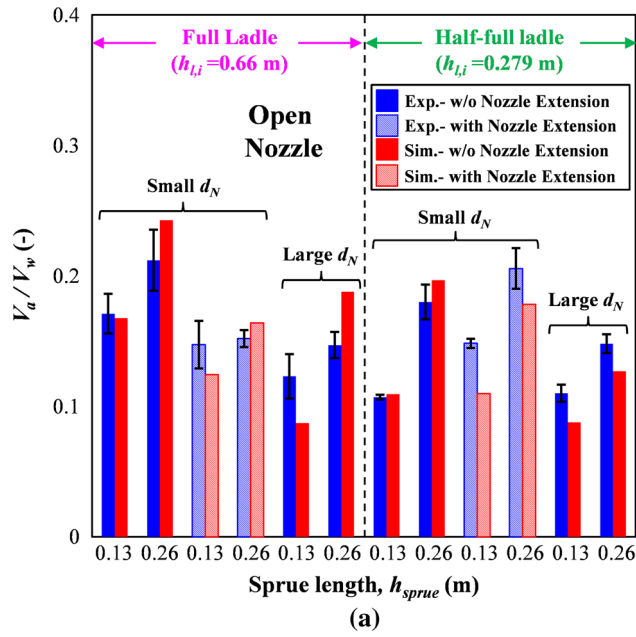


Fig. 10—Comparison of the predicted relative entrained air volumes with measurements for 24 bottom pour ladle configurations: (a) open nozzle, and (b) throttled nozzle.

Figure 10 compares the total volume of entrained air per volume of water poured for all open (Figure 10(a)) and throttled (Figure 10(b)) bottom pour ladle cases. The standard deviations in Figure 10 are calculated based on the three measured relative air entrainment volumes for each configuration. The comparison between the predicted values and experimental measurements shows overall excellent agreement. However, some discrepancies can be observed for the throttled cases.

The standard deviation from the experimental results indicates that the throttled configurations have the largest variations in the measurements. Moreover, some of the measurement results of the throttled

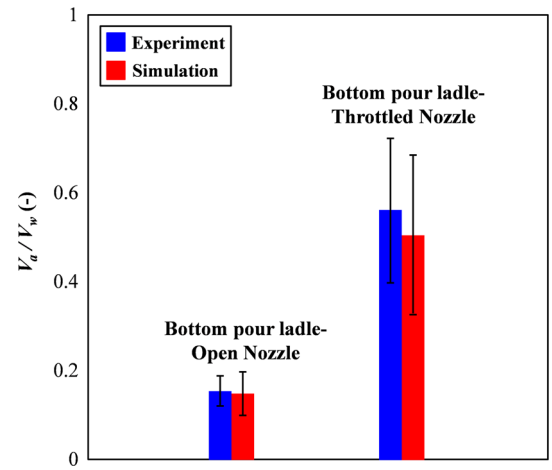


Fig. 11—Comparison of the average predicted and measured total relative entrained air volumes for open and throttled nozzle configurations.

configurations contradict previous findings of different experiments. For example, an increase in the sprue length reduces the air entrainment for the full ladle, large nozzle diameter and also for the half-full ladle, small nozzle diameter without nozzle extension cases. The authors believe that the complex behavior of the throttling process cannot be solely modeled by applying a single turbulence intensity at the nozzle exit. In addition, a throttled nozzle reduces the effective nozzle cross-sectional area, which has not been accounted for in the simulations.

Comparing Figures 10(a) and (b), the throttled nozzle configurations entrain significantly more air than the open nozzle. Throttling the nozzle results in relative entrained air as high as 1 cubic meter of air per cubic meter of water poured. Obviously, the turbulence level of the plunging liquid jet has a significant effect on the air entrainment.

The results also show that due to the higher velocity at the nozzle exit, the full ladle configurations entrain more air than the half-full ladle cases.

Comparison between the small nozzle diameter and large nozzle diameter configurations indicates that increasing the stream diameter reduces the relative air entrainment volume. A larger nozzle diameter produces a higher flow rate and reduces the filling time. Additionally, according to Table I, the nozzle friction is greater for the large nozzle diameters than the small nozzle diameters. This results in even lower water jet velocities at the nozzle exit for the large nozzle diameter cases, which further reduces the air entrainment.

Figure 10 also shows that increasing the drop height of the impinging water from the nozzle increases the relative air entrainment volume. A longer sprue implies a larger drop height, which increases the water jet velocity at the impact location and, hence, the volume of entrained air.

The nozzle extension affects the open nozzle and throttled nozzle cases differently. For the open nozzle configurations, adding an extension to the exit of the nozzle applies more friction to the plunging liquid jet.

The calculated friction coefficients, presented in Table I, reflect this fact. This reduces the velocity of the stream exiting the nozzle extension and, therefore, the air entrainment. For the throttled nozzle cases, a nozzle extension reduces the effect of turbulence intensity. This is because the walls of the nozzle extension eliminate the free surface disturbances on the liquid jet periphery, which are generated at the nozzle exit before the extension; this in turn reduces the air entrainment. On the other hand, for both the open and throttled configurations, when a nozzle extension was used, the ladle was raised to maintain the height of the free falling jet. This increases the liquid velocity at the extension exit, which increases air entrainment. Therefore, the advantages of lower velocities due to an increase in nozzle friction for the open nozzle configurations and the reduction of turbulence intensity for the throttled cases are reduced by the effect of higher velocities at the jet impingement point caused by the increase in total head height. The simulation results, in Figure 10, show that the relative air entrainment volume is larger for the configurations without a nozzle extension.

It is important to point out that the open nozzle configuration with half-full ladle, large nozzle diameter, and short sprue entrains the least amount of air. A comparison of the 24 bottom pour ladle configurations shows that the amount of entrained air differs by a factor of nearly 10 between the cases with least and most entrained air.

Figure 11 compares the average of the experimental measurements and predicted relative air entrainment of the bottom pour ladle cases. An excellent agreement is obtained between the average measured and predicted relative air entrainment volumes. The results indicate that throttling the nozzle can increase the entrained air by more than three times. Therefore, the turbulence level of the liquid at the ladle exit has the most notable effect on the air entrainment. The calculated standard deviations, shown in Figure 11, demonstrate the throttled nozzle configurations have the largest variations in the measurements and predictions.

VI. CONCLUSIONS

The air entrainment model recently developed by the authors is validated for water modeling experiments. Overall, good agreement is achieved between the predicted and the measured relative air entrainment volumes. Results indicate that reducing the total head height and adding a nozzle extension to the end of the

nozzle reduces the air entrainment during filling. In addition, increasing the nozzle diameter increases the volumetric water flow rate, which reduces the pouring time and, therefore, the entrained air volume. The nozzle opening has the most significant effect upon the air entrainment. A throttled nozzle applies large turbulence intensity to the flow at the nozzle exit, markedly increasing the air entrainment volume. Clearly, producing clean castings requires the nozzle to be fully opened during pouring. The promising results obtained in this study further validate the developed air entrainment model.

Future work will link the present air entrainment model to an inclusion generation and transport model, where the final oxide inclusion size and location can be predicted.

REFERENCES

1. J. Campbell: *Complete Casting Handbook*, 1st ed., Butterworth-Heinemann, Oxford, UK, 2011.
2. A.J. Melendez, K.D. Carlson, and C. Beckermann: *Int. J. Cast Met. Res.*, 2010, vol. 23, pp. 278–88.
3. D.R. Askeland, P.K. Trojan, and R.A. Flinn: *AFS Trans.*, 1972, vol. 80, pp. 349–58.
4. J. Campbell: *Mater. Sci. Tech.*, 2006, vol. 22, pp. 127–45.
5. M. Divandari and J. Campbell: *Aluminum Trans.*, 2000, vol. 2, pp. 233–38.
6. T.J. Lin and H.G. Donnelly: *AICHE*, 1966, vol. 12, pp. 563–71.
7. A.K. Biñ: *Chem. Eng. Sci.*, 1993, vol. 48, pp. 3585–30.
8. D.A. Ervine, E. McKeough, and E.M. Elsayy: *ICE Proc.*, 1980, vol. 69, pp. 425–45.
9. K.J. Sene: *Chem. Eng. Sci.*, 1988, vol. 43, pp. 2615–23.
10. E. Van de Sande and J.M. Smith: *Chem. Eng. Sci.*, 1976, vol. 31, pp. 219–24.
11. T. Brattberg and H. Chanson: *Chem. Eng. Sci.*, 1998, vol. 24, pp. 4113–27.
12. C. Wanstall, J. Griffin and C.E. Bates: *Proc. 47th SFSA Technical and Operating Conference*, Chicago, IL, 1993, Paper No. 1.1.
13. C.E. Bates and J. Griffin: Research report no. 106, Steel Founders' Society of America (SFSA), Crystal Lake, IL, USA, 1994.
14. S. Kuyucak: *AFS Trans.*, 2006, vol. 114, pp. 811–18.
15. T. Wang, S. Yao, Q. Tong, and L. Sui: *J. Manuf. Process*, 2017, vol. 27, pp. 108–13.
16. M. Afsharpour, B. Homayun, and S.M.A. Boutorabi: *Mater. Sci. Tech.*, 2014, vol. 30, pp. 152–59.
17. J. Ma, A.A. Oberai, D.A. Drew, R.T. Lahey, and M. Hyman: *J. Comput. Multiphase Flow*, 2011, vol. 3, pp. 41–56.
18. S.H. Majidi and C. Beckermann: *Int. J. Cast Met. Res.*, 2017, vol. 30, pp. 301–15.
19. *MAGMASoft*, MAGMA GmbH, Kackerstrasse 11, 52072 Aachen, Germany.
20. F. White: *Fluid Mechanics*, 7th ed., McGraw Hill Higher Education, New York, USA, 2010.